PAPER • OPEN ACCESS

Accelerated dynamic light sheet microscopy: unifying time-varying patterned illumination and low-rank and sparsity constrained reconstruction

Journal of Physics: Photonics

PAPER

Accelerated dynamic light sheet microscopy: unifying time-varying patterned illumination and low-rank and sparsity constrained reconstruction

Marco Tobia Vitali[1], **Alessia Candeo**[1,*], **Andrea Farina**[2], **Paolo Pozzi**[1], **Alessia Brix**[3], **Andrea Bassi**[1] and **Teresa M Correia**[4,5]

[1] Dipartimento di Fisica, Politecnico di Milano, Piazza Leonardo da Vinci 32, I-20133 Milano, Italy
[2] Istituto di Fotonica e Nanotecnologie, Consiglio Nazionale delle Ricerche, Piazza Leonardo da Vinci 32, I-20133 Milano, Italy
[3] Dipartimento di Biotecnologie Mediche e Medicina Traslazionale, Universitá degli Studi di Milano, LITA, Via Fratelli Cervi 93, 20054 Segrate, Italy
[4] Centre of Marine Sciences (CCMAR), Universidade do Algarve, Campus de Gambelas, 8005-139 Faro, Portugal
[5] School of Biomedical Engineering and Imaging Sciences, King's College London, SE1 7EH London, United Kingdom
[*] Author to whom any correspondence should be addressed.

E-mail: alessia.candeo@polimi.it

Keywords: light sheet, low-rank, sparsity, digital micro-mirror device, Hadamard patterns

Supplementary material for this article is available online

OPEN ACCESS

RECEIVED
11 November 2024

REVISED
10 January 2025

ACCEPTED FOR PUBLICATION
21 January 2025

PUBLISHED
10 February 2025

Abstract

Light Sheet Fluorescence Microscopy (LSFM) enables rapid and gentle 3D fluorescence imaging of dynamic processes over extended periods in translucent samples at the mesoscopic scale. However, its temporal resolution is constrained by the sequential acquisition of individual two-dimensional planes at varying depths, making it challenging to capture rapid dynamics such as the beating of a zebrafish heart. To address this limitation, we recently developed spatially modulated Selective Volume Illumination Microscopy, which utilizes a compressed sensing approach to reconstruct the entire imaging volume from measurements where multiple planes are illuminated simultaneously using spatially modulated light. Building on this advancement, we now introduce a novel spatio-temporal patterned illumination strategy and volume reconstruction method that incorporates low-rank and sparsity constraints, effectively leveraging the temporal and spatial redundancy present in sequential volumetric acquisitions. This method was applied to the volumetric imaging of embryonic zebrafish hearts, achieving an improvement in imaging speed of 4-fold compared to standard LSFM and a 2-fold improvement compared to traditional compressed sensing approaches, while preserving reconstruction accuracy and enabling the visualization of fast dynamic events with a resolution of a few tens of milliseconds. Our approach represents a step forward in enhancing the temporal resolution of LSFM for studying fast biological dynamics.

1. Introduction

The demand for fast high-resolution imaging solutions for monitoring live biological specimens has continuously driven innovations in optical microscopy. Light Sheet Fluorescence Microscopy (LSFM) has emerged as a tool of choice for such applications due to its unique ability to illuminate a thin section of the specimen while minimizing exposure to excitation light, thereby preserving the sample over extended periods of time [1]. However, traditional scanning methods employed in LSFM, while effective, face limitations in temporal resolution and throughput when tasked with volumetric imaging of fast dynamic events. The temporal resolution of conventional LSFM setups is limited by the need to mechanically translate either the sample, excitation beam or detection objective. Several approaches have been proposed to overcome this limitation. For example, Fahrbach *et al* [2] solved this problem using tunable optic elements to move the detection focus plane on the scanning illumination sheet. Their microscope had no moving parts and allowed imaging several volumes per second. The combination of Swept Confocally-Aligned Planar Excitation

microscopy with a high-speed camera was used to achieve acquisition speeds beyond 100 volumes s^{-1} [3]. A promising direction to circumvent these limitations involves the use of volumetric illumination strategies, where the whole sample volume is illuminated simultaneously with spatially modulated light. This approach can enhance imaging speed by parallelizing the acquisition, a feature critical for real-time observation of dynamic biological processes. In particular, we recently introduced spatially modulated Selective Volume Illumination Microscopy (sm-SVIM) [4], an LSFM-based approach where a digital micromirror device (DMD) is used to simultaneously illuminate several planes within the depth of field of the detection optics. Then, by exploiting the sparsity/compressibility of biological images or their spatial features, a compressed sensing method is used to reconstruct a volumetric image from fewer measurements than the number of individual planes in the volume, thus expediting the imaging process without sacrificing image quality. More recently, low-rank (LR) matrix completion methods have became popular in the context of dynamic imaging. These methods extended the idea of compressed sensing to matrices, allowing to effectively exploit the redundancy along the temporal dimension in, for example, dynamic medical imaging applications [5–8].

Building upon these recent advancements, our work introduces a solution to accelerate acquisitions and achieve efficient time-lapse reconstruction, which combines (spatio-temporally modulated) compressed acquisition and LR completion methods. More specifically, by selectively acquiring data points of the sample, illuminated with structured light, we propose a method that captures fast volumetric dynamic biological events, while reducing the amount of acquired data. This methodology enhances the quality of high-resolution volumetric reconstruction and paves the way for fast dynamic imaging of biological systems at the microscopic scale.

2. Materials and methods

2.1. Optical imaging setup

The volume of interest is illuminated with different patterns using a DMD (Texas Instruments DLP6500FLQ), an efficient and inexpensive intensity spatial light modulator. DMDs feature an array of micrometric mirrors that can be individually tilted. As a result, light shining on the DMD can be deflected by each mirror along two different paths. The sample is positioned on one of these paths, so that by tilting each mirror the sample can be dynamically illuminated with a binary amplitude modulation mask creating a patterned illumination. A relay system is used to conjugate the DMD to the sample planes to illuminate the sample with the pattern created by the bright and dark pixels of the DMD (figure 1(a)).

More specifically, the illumination pattern is created along the axial direction of the detection using a light sheet-like configuration: the sample is illuminated by thin planes of light that are orthogonal to the detection axis. Due to hardware constraints, the DMD pixels are oriented at a 45° angle. In the experiments we use 4 columns of rotated DMD pixels to create a single light sheet with a thickness of 4.78 μm at the sample plane. For our volumetric acquisitions, we use 16 light sheets to create a combined illumination that covers 76 μm along the z-axis. These light sheets are independently activated or deactivated by the DMD based on a scheme defined by the columns of scrambled Hadamard patterns. Figure 1(b) shows a possible DMD configuration that generates a modulated illumination with 16 on or off light sheets. To complete a full acquisition, 16 different frames (patterns) are recorded. For each frame f, the light sheets are switched on or off according to the binary values (1 or 0) in the corresponding fth column of the scrambled Hadamard pattern (described in section 2.3), as demonstrated in figure 1(c). By applying compression techniques, we can reduce the number of columns (number of patterns) but not rows (number of light sheets)

A 20× objective (Nikon, 0.45 NA) is used for detection, while illumination magnification from the DMD to the sample was $M_{exp} = 8.94$ (given by the lenses L2, L3, TL1 and illumination objective in figure 1(a)). The list of the parts used for the setup is shown in table 1. For the reported results, a subregion of the DMD of 810 × 96 pixels was used, obtaining an extension of the illumination pattern of 690 μm across the camera width (Y axis in figure 1(a)) and 76 μm along the axial direction (Z axis in figure 1(a)). The axial extent of illumination was adjusted to match the thickness of the tissue under study, as well as the effective depth of field of the detection objective in experimental conditions. This can be done by changing the relay system and the objective, or it can be tuned by using a different active area on the DMD. Typical range values span from 76 μm to 200 μm. The active area of the camera (Hamamatsu Orca Flash 4.0 V2) was limited to 87 μm on the X axis to reduce the frame acquisition time and obtain the desired from rate, at a final sampling of 2048 pixels on the Y axis and 256 pixels on the X axis. The patterns applied to the DMD are structured in discrete lines, only modulating light in the axial direction.

Differently from our previous sm-SVIM implementations that used an incoherent LED source [4, 9], here, a laser source is used to illuminate the sample. To take advantage of the high intensity of the laser source, while avoiding artefacts entailed by coherent illumination, a continuous wave diode laser coupled to a multimode optical fibre is used. The large core of this fibre (200 μm) deteriorates the laser coherence. The

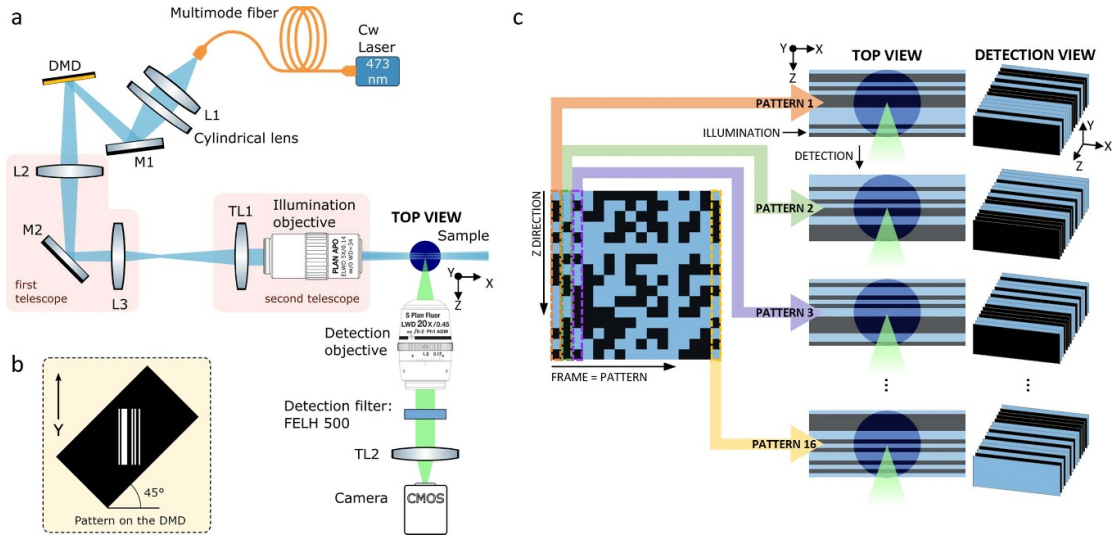

Figure 1. Experimental setup. (a) Spatially modulated Selective Volume Illumination Microscope based on a digital micro-mirror device (DMD) to simultaneously illuminate several sample planes. Other components: CW laser; multimode fiber; L1, L2, L3 Lenses; M1, M2 mirrors; TL1, TL2 tube lens; illumination objective; detection objective; detection filter; CMOS camera. (b) Schematic of the DMD patterns used to create modulated illumination along the z-axis. (c) Example of the scrambled Hadamard patterns used for one volumetric acquisition. The patterns change randomly at each volumetric acquisition (time frame).

Table 1. Component list. Main specifications of the components used in the experimental setup.

Component	Specification
CW laser	473 nm, 40 mW
MM fiber	200 μm core diameter
L1	$f_1 = 30$ mm
Cyl. lens	$f_{CL} = 300$ mm (y axis)
DMD	Texas Instruments DLP6500, 7.56 μm $\times$ 7.56 μm mirrors
L2	$f_2 = 150$ mm
L3	$f_3 = 75$ mm
TL1	$f_{TL1} = 180$ mm
Ill. obj.	$f_{I.O.} = 40$ mm, NA $= 0.14$
Det. obj.	Nikon 20$\times$, NA $= 0.45$
Det. filter	FELH500, longpass at 500 nm
TL2	Nikon, $f_{TL2} = 200$ mm
Camera	Hamamatsu ORCA-Flash4.0 V2, 6.5 μm $\times$ 6.5 μm pixels, 100 fps, 2048 $\times$ 2048 px active sensor

fiber tip is imaged on the DMD (lens L1) with a cylindrical lens added to preferably illuminate the active region of the DMD, which is more extended in the vertical direction (Y) than in the horizontal (Z) direction.

Patterns like those presented in figure 1(c) were generated and uploaded to the DMD at the beginning of each measurement. The whole microscope is controlled using *ScopeFoundry*, a Python-based software that controls both data acquisition and visualization [10]. ScopeFoundry allows interaction with the hardware and execution of custom-designed measurements (https://github.com/marccv/smSVIM).

Sm-SVIM microscopy requires a sufficiently large detection depth of field to uniformly integrate the emitted fluorescence along the Z direction. Tomer *et al* [11] devised a SPherical-aberration-assisted Extended Depth-of-field light sheet microscope where both sample and detection objective were kept stationary while the light sheet was scanned within the detection depth of focus. The depth of focus was purposefully extended in the axial direction (i.e. Z-axis) by introducing spherical aberrations in the detection path. For this purpose, a layer of medium with refractive index higher than air (for objectives that are aberration-corrected in air) was inserted between the sample and the detection objective. The Point Spread Function (PSF) axial Full Width at Half Maximum increased with the layer's refractive index and thickness. In the reported measurements, samples (zebrafish embryos) were enclosed in 2% agarose (see section 2.2) and then lowered in a quartz cuvette filled with distilled water. The glass of the cuvette was 1.30 mm thick and the water was confined in a square of 10 $\times$ 10 mm^2. The depth of field, of the reported setup in these conditions, was sufficiently large to uniformly image our volume of interest (with a Z extent of 76 μm),

without the need of additional high refractive index layers. The elongation of the PSF was caused by intrinsic aberrations in the detection arm, as the detection objective employed is designed to work in air.

2.2. Sample preparation

Tg(kdrl:eGFP)s843 zebrafish embryos, expressing green fluorescent protein (GFP) in the vascular structure were imaged at 3–5 d post fertilization (dpf). The transgenic zebrafish lines and sample preparation protocol are described in detail in Bassi *et al* [12]. Briefly, zebrafish were kept in 0.003% 1-phenyl-2-thiourea (PTU) to inhibit the melanization of tissues. To reduce the movement of the fish during data acquisition, samples were anesthetized by placing them in 0.016% tricaine (Ethyl 3-aminobenzoate methanesulfonate salt) and restrained in low melting point 2% agarose gel. The liquid gel with the sample was drawn into a capillary so that after its solidification we could extrude an agarose cylinder. During acquisitions, we lowered the sample in the cuvette, which was filled with fish water (Instant Ocean, 0.1% Methylene Blue).

2.3. Sampling strategy

Our sm-SVIM was used to perform volumetric measurements of the beating zebrafish heart. Fluorescence intensity is the product of the illumination intensity and fluorophore concentration. A volume illumination modulated in the Z direction is projected onto the sample and each pixel of the CMOS camera integrates all the fluorescent emission generated within the PSF of the detection objective. As a consequence, each pixel acts as a single-pixel detector [13] collecting all the light coming from the different modulated planes in the Z direction at a fixed X–Y position. By projecting different patterns lying in a suitable basis set, such as Hadamard, Bernoulli, Gaussian, Wavelet, etc, and solving an inverse problem similar to single pixel camera applications, it is possible to reconstruct the distribution of the fluorescence emission over the Z dimension for each pixel of the camera, which in turn allows recovering the overall 3D distribution inside the sample.

In this work, scrambled Hadamard patterns were used to illuminate the sample. This basis set, widely used in compressed-sensing multispectral fluorescence imaging [14], merges the advantages of the classical Hadamard basis in terms of filling factor, orthogonality and suitability for binary spatial light modulators, such as DMDs, and the advantages of the random sampling with respect to the compressed-sensing framework. Moreover, to efficiently exploit temporal correlations, time-varying scrambled Hardamard patterns were used, meaning that the patterns are different at each time frame.

Scrambled Hadamard patterns are obtained by randomly permutating the rows and columns of an $N \times N$ Hadamard matrix. The patterns remain orthogonal whilst increasing their randomness, which is essential for compressed sensing-type methods to be effective. By selecting the first $M < N$ rows it is possible to reduce the number of measurements to generate data with different compression ratios.

The Hadamard and, therefore, the scrambled Hadamard matrix have positive and negative entries to preserve orthogonality, but the illumination can only be positive. Thus, two acquisitions were tested:

- *A1 Double Frame*: a pair of complementary positive patterns was projected sequentially on the sample. In this case, the real pattern can be obtained by subtracting the pair of measurements. Thus, before the image reconstruction, the respective measurements have been subtracted.
- *A2 Single Frame*: the negative values have been set to zero and one positive acquisition per pattern has been performed.

The first modality is advantageous in terms of background subtraction, but has the drawback of doubling the measurement time. The second has the advantage of not increasing the acquisition time, but it is more sensitive to background and to illumination fluctuations.

2.4. Image reconstruction methods

The data to be reconstructed consists of $n_V \times n_H \times N \times T$, where n_V and n_H are the numbers of vertical and horizontal pixels on the camera, respectively, N is the Hadamard order representing the number of sections in the Z dimension, and T are the time points. In this work, three reconstruction methods have been applied for different compression ratios.

- **Alternating Direction Method for Multipliers (ADMMs) TV**. This is based on the solution of the following minimization problem:

$$\underset{x}{\operatorname{argmin}} \left\{ \left\| Ex - b \right\|_2^2 + \lambda_1 \mathrm{TV}(x) \right\}, \tag{1}$$

  where $\|\cdot\|_2$ is the L2-norm, $E = AH$ is the operator containing the full $N \times N$ scrambled Hadamard matrix H and an (undersampling) operator A that selects the first M rows of H depending on the particular compression ratio used, b is the experimental data, $\mathrm{TV}(x)$ is the 3D Total Variation operator applied to the spatial

dimensions, thus enforcing sparsity in the spatial gradient domain, and λ_1 is the regularization parameter for the TV regularization term [15, 16]. The problem (1) is solved through the ADMMs [17].

- **ADMM LR + S**. The main idea of Robust Principal Component Analysis, or LR plus sparse matrix decomposition, is to separate the original image series into the temporally correlated background (L) and the sparse dynamic information (S) [18–20]. Thus, the LR plus sparse (LR + S) image reconstruction problem is formulated as:

$$\underset{L,S}{\operatorname{argmin}} \left\{ \left\| E(L+S) - b \right\|_2^2 + \lambda_L \left\| L \right\|_* + \lambda_S \left\| \Psi S \right\|_1 \right\}, \tag{2}$$

where $\|\cdot\|_*$ is the nuclear norm, i.e. the sum of the singular values, $\|\cdot\|_1$ is the L1-norm, Ψ is a sparsifying transform (temporal Fourier transform). The regularization parameters λ_L and λ_S balance the contribution of the LR L and sparse S components, respectively. The LR constraint was applied on a spatio-temporal *Casorati* matrix, and thus, volumes, with M voxels, at different time points were flattened into a matrix with M rows and T columns. Equation (2) is solved, as before, using the ADMM method.

- **ADMM TV + LR**. This method is based on the ADMM TV method with an added LR regularization term acting along the temporal dimension [5, 7]. The problem is formulated as follows:

$$\underset{x}{\operatorname{argmin}} \left\{ \left\| Ex - b \right\|_2^2 + \lambda_1 \mathrm{TV}(x) + \lambda_2 \left\| x \right\|_* \right\}. \tag{3}$$

As before, a Casorati matrix is constrained to have LR. Thus, the second regularization term was built on the hypothesis that time points are mutually correlated because they follow a sufficiently slow movement of a given structure. On the other hand, the first regularization term exploits spatial sparsity, as in the ADMM TV method. The ADMM method is also used for solving equation (3).

2.5. Evaluation

The three image reconstruction methods and time varying scrambled Hadamard accelerated acquisition were tested using dynamic images of embryonic zebrafish beating hearts. The zebrafish heart has a beating frequency of 2–4 Hz and is approximately 200 μm long and 100 μm in diameter, making a volumetric acquisition in a few tens of milliseconds desirable. The camera was operating at 386 frames per second with an exposure time limited to 1.2 ms in order to reduce artefacts due to the DMD switching. The imaged volume had a final size of $87 \times 690 \times 76$ μm.

To evaluate the performance of the different methods, three different experiments were performed:

- *Experiment 1*: A fully sampled (FS) dataset was acquired using the A1 *Double Frame* approach, consisting of a total of $T = 12$ volumes, each acquired in 82 ms by alternating a total of $N = 16$ scrambled Hadamard patterns, each repeated twice in order to perform double frame reconstruction, therefore resulting in 32 DMD patterns. Compressed data were retrospectively generated by undersampling the FS dataset, obtaining acceleration factors of 2-, 4- and 8-fold for the A1 *Double Frame* approach (by keeping 1/2, 1/4, and 1/8 of the acquired scrambled Hadamard patterns, respectively).
- *Experiment 2*: A 2-fold and a 4-fold prospectively accelerated dataset were acquired in real conditions (i.e. not undersampled *a posteriori*) using the A1 *Double Frame* approach, consisting of a total of $T = 25$ and $T = 50$ volumes, acquired in 41.41 ms and 20.71 ms, respectively.
- *Experiment 3*: A 2-fold and 4-fold prospectively accelerated dataset were acquired in real conditions (i.e. not undersampled *a posteriori*) using the A2 *Single Frame* approach, consisting of a total of $T = 50$ and $T = 50$ volumes, acquired in 20.71 ms and 10.35 ms, respectively.

Experiment 1 provided a FS A1 *Double Frame* dataset, and thus, enabled the generation of restrospectively undersampled data, optimization of the reconstruction parameters and quantitative assessment of image quality. The quality of the images obtained from retrospectively undersampled data using the different image reconstruction methods was compared with the FS image using the mean squared error (MSE) and structural similarity index (SSIM) quantitative metrics.

The minimization problems in equations (1)–(3) were solved using the ADMM algorithm, which relies on a nested conjugate gradient (to solve the linear sub-problem), with stopping criteria based on the maximum number of iterations (50) and relative tolerance (0.0009) for the outer loop and with a maximum of 3 iterations and 0.0001 tolerate for the inner conjugate gradient loop. The optimal ADMM parameters were selected as the ones that minimize the MSE. All reconstructions were run on a Windows laptop with an Intel(R) Core(TM) i7-8650U CPU.

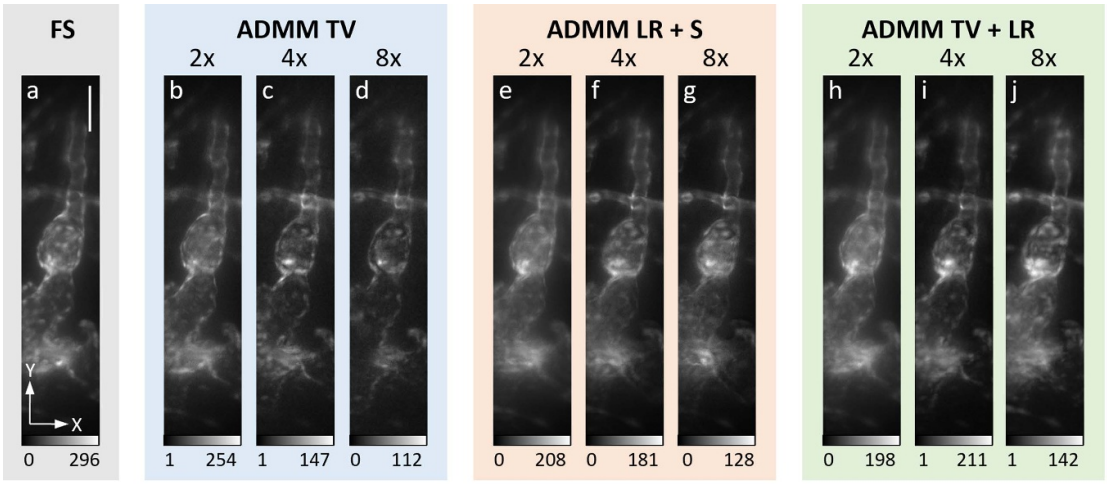

Figure 2. Experiment 1 - A1 *Double Frame* retrospective study. (a) Fully sampled (FS) image and reconstructions obtained using the ADMM with (b)–(d) Total variation (ADMM TV), (e)–(g) Low-rank plus Sparse (ADMM LR + S), and (h)–(j) Total Variation and Low-Rank (ADMM TV + LR) methods, from 2-, 4-, and 8-fold retrospectively undersampled data (generated from the fully sampled dataset). Images show a maximum intensity Z-projection (Z-MIP) for a single time frame, which corresponds to an image showing for each *XY* position the maximum value along the *Z*-axis. The scale bar represents 50 μm.

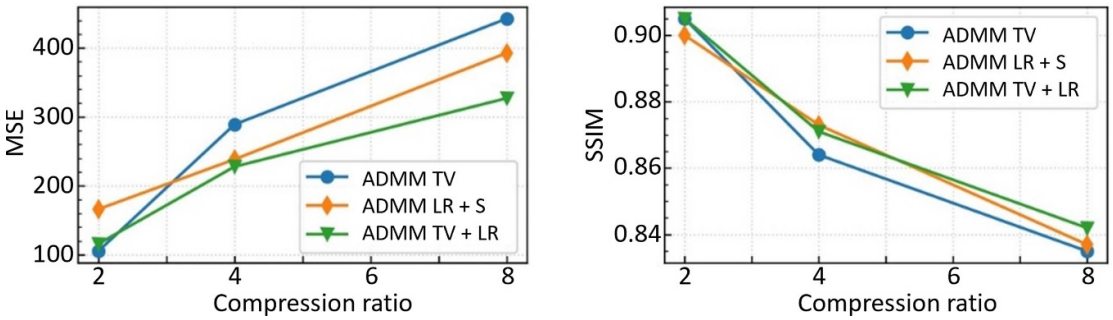

Figure 3. Experiment 1 - Image quality. Mean squared error (MSE) and structural similarity index (SSIM) obtained for the images reconstructed from 2×, 4×, and 8× retrospectively undersampled data using the different reconstruction methods.

3. Results

Images were reconstructed from dynamic data of zebrafish embryos' beating hearts using the three methods described in section 2.4.

Figure 2 shows the zebrafish embryo heart images reconstructed from Experiment 1, i.e. from retrospectively undersampled data at various compression ratios (2×, 4×, 8×), using the A1 *Double Frame* approach, and FS image, reconstructed from the FS dataset A1 (no compression). Complete videos slowed down 5 times of the FS and of the TV + LR methods are available as supplementary materials (supplementary video 1–4). Figure 3 shows the corresponding image quality metrics. Quantitatively, at 4- and 8-fold acceleration rates, images obtained with ADMM TV exhibit a lower SSIM (and higher MSE) when compared to the ADMM LR + S and TV + LR methods. The average reconstruction time for ADMM TV, ADMM LR + S, ADMM TV + LR was 21 min, 4 min, and 9 min, respectively.

The images obtained from prospectively A1 *Double Frame* measurements (Experiment 2) are shown in figure 4, while complete videos slowed down 5 times of the TV + LR methods for the 2× and 4× compression ratios are available as supplementary materials (supplementary video 5 and 6). Reconstructions at 2× acceleration maintain high quality across all methods. However, at 4× acceleration, the quality noticeably diminishes, particularly in the axial reconstruction of the zebrafish hearts. However, the ADMM TV+LR method provides good image quality indicating that this method could be suitable to achieve higher acceleration rates. This observation is consistent with the quantitative metrics obtained in Experiment 1 (shown in figure 3), which highlight the enhanced accuracy of ADMM TV + LR at higher acceleration rates.

A possible alternative to accelerate acquisitions is to use the A2 *Single Frame* scheme (Experiment 3), which consists of the reconstruction of only a set of positive patterns, thus requiring the acquisition of half

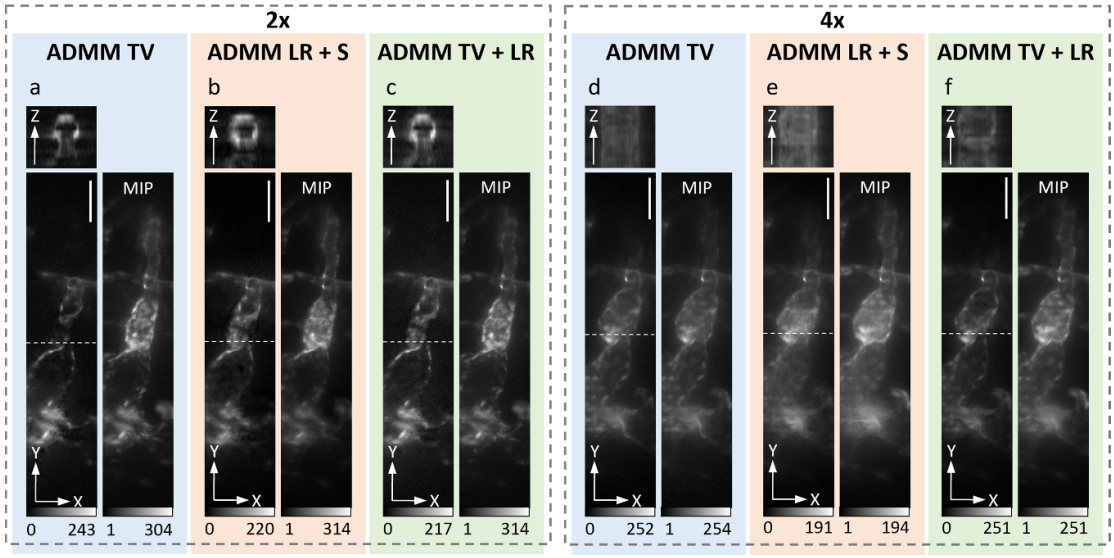

Figure 4. Experiment 2 - A1 *Double Frame* prospective study. Reconstructions obtained using the ADMM with Total variation (ADMM TV), Low-rank plus Sparse (ADMM LR + S), and Total Variation and Low-Rank (ADMM TV + LR) methods, from (a)–(c) 2- and (d)–(f) 4-fold prospectively undersampled data acquired in real conditions (i.e. not undersampled *a posteriori*). Images show a single Z-stack slice, a single Y-stack slice and maximum intensity Z-projection (MIP) for a single time frame. The scale bar represents 50 μm.

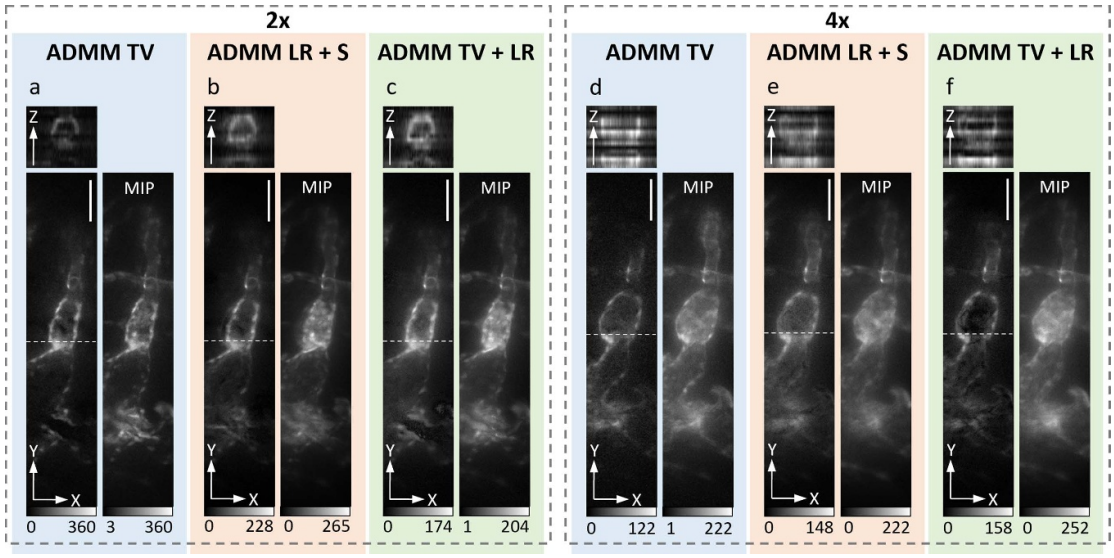

Figure 5. Experiment 3 - A2 *Single Frame* prospective study. Reconstructions obtained using the ADMM with Total variation (ADMM TV), Low-rank plus Sparse (ADMM LR + S), and Total Variation and Low-Rank (ADMM TV + LR) methods, from (a)–(c) 2- and (d)–(f) 4-fold prospectively undersampled data acquired in real conditions (i.e. not undersampled *a posteriori*). Images show a single Z-stack slice, a single Y-stack slice and maximum intensity Z-projection (Z-MIP) for a single time frame. The scale bar represents 50 μm.

the patterns required for A1 *Double Frame*, doubling the volume acquisition rate. We observe that applying the A2 *Single Frame* scheme at 2× acceleration (figures 5(a)–(c)) competes with the speed of 4× acceleration obtained with the A1 method while preserving the quality of reconstruction (figures 5(d)–(f)). Even though the A2 *Single Frame* method yields satisfactory outcomes at 2× acceleration, it exhibits some artefacts at 4×. The complete videos slowed down 5 times of the TV + LR methods for the 2× and 4× accelerations and *Single Frame* scheme are available as supplementary materials (supplementary video 7 and 8).

4. Discussion

Spatially modulated light has been used in LSFM to improve spatial resolution [21, 22] and combined with spatial compressed sensing to accelerate acquisitions [4]. Here, spatially and temporally modulated

illumination patterns were combined with LR and sparsity constrained reconstruction to improve the temporal resolution of LSFM and enable real-time visualization of fast dynamic events, such as the beating zebrafish heart. Thus, we compared the performance of three image reconstruction methods, including the traditional ADMM TV (spatial sparsity), and the two novel approaches ADMM LR + S (LR and temporal sparsity) and ADMM TV + LR (LR and spatial sparsity) using retrospectively and prospectively undersampled dynamic data.

For 2-fold retrospectively undersampled data (Experiment 1), the different image reconstruction methods produced similar results, without obvious visual differences. However, ADMM LR + S and ADMM TV + LR provide images that are qualitatively and quantitatively superior to ADMM TV for 4- and 8-fold undersampled data. Thus, higher compressibility is offered by these methods, and thus, higher reconstruction performance is achieved than when using spatial sparsity alone. The MSE and SSIM values indicate that ADMM TV + LR provides images that are quantitatively superior to ADMM LR + S, which is likely due to the fact that spatial sparsity regularization helps limit the noise amplification (spatial denoising effect) due to undersampling. ADMM LR + S and ADMM TV + LR also generate good quality images from prospectively A1 undersampled acquisitions (Experiment 2).

ADMM LR + S and TV + LR have similar SSIM scores for retrospective reconstructions, but ADMM TV + LR demonstrates a notably lower MSE, indicating its prowess in maintaining structural integrity akin to LR + S while ensuring superior pixel-accuracy in reconstructions. Thus, ADMM TV + LR stands out as the most balanced approach, combining structural fidelity with error minimization. However, ADMM LR + S generates good quality images in a shorter amount of time. Nevertheless, a fast ADMM algorithm [23] can be used to accelerate all image reconstruction methods by approximately 2×. However, it still involves a traditional iterative non-linear approach, which is still not ideal for real-time imaging. This well-known disadvantage of iterative reconstruction methods has motivated recent advances in deep learning-based image reconstruction schemes, which we will explore, in the future, to achieve real-time image reconstruction times [24].

Prospective acquisitions performed using the A2 *Single Frame* scheme (Experiment 3) enable 2× faster acquisitions compared to the A1 *Single Frame* method. However, the obtained images exhibit artefacts along the *Z* axis, particularly at 4-fold acceleration. Therefore, for the A2 acquisition scheme, 2× acceleration is the preferred choice, offering reconstructions with image quality and time efficiencies similar to A1 at 4× acceleration.

Results from both qualitative and quantitative analysis indicate that adding LR (temporal) regularization was pivotal to achieving higher acceleration rates, and thus, to enable high-quality reconstruction from as little as 2 illumination patterns (8× acceleration). Hence, the proposed acquisition and reconstruction strategy enables the reduction of the number of acquired measurements, and thereby the reduction of light exposure and motion during the acquisition of a single volume, whilst preserving the quality of the reconstruction images, and thus, offering new possibilities to measure fast dynamic events with a few tens of ms resolution.

By making the acquisition faster, this approach is particularly valuable for dynamic imaging and developmental studies of highly motile samples, such as cnidarians (e.g. *Hydra vulgaris* or corals), which exhibit rapid and continuous movement, particularly in earlier development stages. To conduct behavioral studies under conditions that minimally disrupt the experiment and maintain optimal physiological states, these animals should not be anesthetized. However, imaging under such conditions poses significant challenges, particularly when tracking fast processes such as calcium signaling. In particular, as demonstrated here, it allows imaging the rapid contraction and relaxation of the zebrafish heart across different developmental stages and can offer critical insights into cardiac development and *in vivo* function. One drawback of this approach is the relatively long reconstruction time, which currently limits the ability to inspect samples in real time. However, this limitation could be addressed—and even overcome—by leveraging deep-learning-based reconstruction techniques for real-time analysis, as demonstrated in our previous work [24].

5. Conclusions

A spatially and temporally varying patterned illumination strategy and LR and sparsity constrained reconstruction approach has been proposed to enable 3D LSFM imaging of fast dynamic events, such as the beating heart of live embryonic zebrafish. More specifically, time varying scrambled Hadamard patterns are used to accelerate acquisitions and high quality images are generated using an image reconstruction method with LR and sparsity constraints, which efficiently exploit temporal correlations and spatial sparsity. The proposed spatio-temporal patterned illumination and LR and sparsity constrained reconstruction showed promising results in both retrospective and prospective acceleration studies, indicating that this method can

be used to improve temporal resolution by approximately 8 times, and thus, providing sufficient temporal resolution to visualize 3D dynamic events on the millisecond time scale.

Data availability statement

The data that support the findings of this study are openly available at the following URL/DOI:https://doi.org/10.5281/zenodo.14062483.

Acknowledgments

This study received Portuguese national funds from FCT—Foundation for Science and Technology through projects UIDB/04326/2020 (DOI:https://doi.org/10.54499/UIDB/04326/2020), UIDP/04326/2020 (DOI:https://doi.org/10.54499/UIDP/04326/2020) and LA/P/0101/2020 (DOI:https://doi.org/10.54499/LA/P/0101/2020). This Project received funding from 'la Caixa' Foundation and FCT, I P under the Project code LCF/PR/HR22/00533, European Union's Horizon 2020 research and innovation program under the Marie Skłodowska-Curie OPTIMAR grant with agreement no 867450 (DOI:https://doi.org/10.3030/867450), European Union's Horizon 2020 research and innovation LASERLAB-EUROPE program under grant agreement no. 871124 (DOI:https://doi.org/10.3030/871124), European Union's Horizon Europe Programme IMAGINE under grant agreement no. 101094250 (DOI:https://doi.org/10.3030/101094250) and the European Union's NextGenerationEU Programme with the I-PHOQS Infrastructure (IR0000016, ID D2B8D520, CUP B53C22001750006) 'Integrated infrastructure initiative in Photonic and Quantum Sciences.

ORCID iDs

Marco Tobia Vitali https://orcid.org/0009-0002-1436-0675
Alessia Candeo https://orcid.org/0000-0001-9597-3056
Andrea Farina https://orcid.org/0000-0002-3180-6328
Paolo Pozzi https://orcid.org/0000-0002-3420-8593
Alessia Brix https://orcid.org/0000-0002-2679-9127
Andrea Bassi https://orcid.org/0000-0002-5017-0775
Teresa M Correia https://orcid.org/0000-0002-1606-9550

References

[1] Huisken J, Swoger J, Del Bene F, Wittbrodt J and Stelzer E 2004 Optical sectioning deep inside live embryos by selective plane illumination microscopy *Science* **305** 1007–9
[2] Fahrbach F O, Voigt F F, Schmid B, Helmchen F and Huisken J 2013 Rapid 3D light-sheet microscopy with a tunable lens *Opt. Express* **21** 21010–26
[3] Voleti V *et al* 2019 Real-time volumetric microscopy of *in vivo* dynamics and large-scale samples with scape 2.0 *Nat. Methods* **16** 1054–62
[4] Calisesi G, Castriotta M, Candeo A, Pistocchi A, D'Andrea C, Valentini G, Farina A and Bassi A 2019 Spatially modulated illumination allows for light sheet fluorescence microscopy with an incoherent source and compressive sensing *Biomed. Opt. Express* **10** 5776–88
[5] Tourais J *et al* 2022 High-resolution free-breathing quantitative first-pass perfusion cardiac MR using dual-echo dixon with spatio-temporal acceleration *Front. Cardiovascular Med.* **9** 884221
[6] Lin C Y and Fessler J A 2019 Efficient dynamic parallel MRI reconstruction for the low-rank plus sparse model *IEEE Trans. Comput. Imaging* **5** 17–26
[7] Yao J, Xu Z, Huang X and Huang J 2018 An efficient algorithm for dynamic MRI using low-rank and total variation regularizations *Med. Image Anal.* **44** 14–27
[8] Miao X, Lingala S G, Guo Y, Jao T, Usman M, Prieto C and Nayak K S 2016 Accelerated cardiac cine MRI using locally low rank and finite difference constraints *Magn. Reson. Imaging* **34** 707–14
[9] Calisesi G, Ancora D, Tacconi C, Fantin A, Perin P, Pizzala R, Valentini G, Farina A and Bassi A 2022 Enlarged field of view in spatially modulated selective volume illumination microscopy *Microsc. Microanal.* **28** 1622–31
[10] (Availabel at: http://arxiv.org/abs/http://www.scopefoundry.org)
[11] Tomer R, Lovett-Barron M, Kauvar I, Andalman A, Burns V M, Sankaran S, Grosenick L, Broxton M, Yang S and Deisseroth K 2015 SPED light sheet microscopy: fast mapping of biological system structure and function *Cell* **163** 1796–806
[12] Bassi A, Schmid B and Huisken J 2015 Optical tomography complements light sheet microscopy for in toto imaging of zebrafish development *Development* **142** 1016–20
[13] Duarte M F, Davenport M A, Takhar D, Laska J N, Sun T, Kelly K F and Baraniuk R G 2008 Single-pixel imaging via compressive sampling *IEEE Signal Process. Mag.* **25** 83–91
[14] Ghezzi A, Lenz A J M, Soldevila F, Tajahuerce E, Vurro V, Bassi A, Valentini G, Farina A and D'Andrea C 2023 Computational based time-resolved multispectral fluorescence microscopy *APL Photonics* **8** 046110 1–7
[15] Correia T *et al* 2015 Accelerated optical projection tomography applied to *in vivo* imaging of zebrafish *PLoS One* **10** 1–17
[16] Chambolle A and Pock T 2011 A first-order primal-dual algorithm for convex problems with applications to imaging *J. Math. Imaging Vis.* **40** 120–45

[17] Boyd S, Parikh N, Chu E, Peleato B and Eckstein J 2011 Distributed Optimization and Statistical Learning via the Alternating Direction Method of Multipliers
[18] Candès E J, Li X, Ma Y and Wright J 2011 Robust principal component analysis? *J. ACM* **58** 1–37
[19] Otazo R, Candés E and Sodickson D K 2015 Low-rank plus sparse matrix decomposition for accelerated dynamic MRI with separation of background and dynamic components *Magn. Reson. Med.* **73** 1125–36
[20] Trémoulhéac B, Dikaios N, Atkinson D and Arridge S R 2014 Dynamic mr image reconstruction-separation from undersampled ($\mathbf{k}$, t)-space via low-rank plus sparse prior *IEEE Trans. Med. Imaging* **33** 1689–701
[21] Neil M A A, Juškaitis R and Wilson T 1997 Method of obtaining optical sectioning by using structured light in a conventional microscope *Opt. Lett.* **22** 1905–7
[22] Gustafsson M G L 2005 Nonlinear structured-illumination microscopy: wide-field fluorescence imaging with theoretically unlimited resolution *Proc. Natl Acad. Sci.* **102** 13081–6
[23] Goldstein T, O'Donoghue B, Setzer S and Baraniuk R 2014 Fast alternating direction optimization methods *SIAM J. Imaging Sci.* **7** 1588–623
[24] Obando M, Bassi A, Ducros N, Mato G and Correia T 2023 Model-based deep learning framework for accelerated optical projection tomography *Sci. Rep.* **13** 21735